LASER
& PHOTONICS
REVIEWS

Supporting Information

for *Laser Photonics Rev.*, DOI 10.1002/lpor.202200499

Observation of Square-Root Higher-Order Topological States in Photonic Waveguide Arrays

Juan Kang, Tao Liu, Mou Yan, Dandan Yang, Xiongjian Huang, Ruishan Wei, Jianrong Qiu, Guoping Dong, Zhongmin Yang* and Franco Nori*

Supporting Information for:

Observation of Square-Root Higher-order Topological States in Photonic waveguide arrays

Juan Kang[a,‡], Tao Liu[b,a,‡], Mou Yan[b], Dandan Yang[a], Xiongjian Huang[a], Ruishan Wei[a], Jianrong Qiu[c], Guoping Dong[a,*], Zhongmin Yang[b,*] , Franco Nori[d]

[a] State Key Laboratory of Luminescent Materials and Devices, and Guangdong Provincial Key Laboratory of Fiber Laser Materials and Applied Techniques, Guangdong Engineering Technology Research and Development Center of Special Optical Fiber Materials and Devices, School of Materials Science and Engineering, South China University of Technology, Guangzhou 510640, China

[b] School of Physics and Optoelectronics, South China University of Technology, Guangzhou 510640, China

[c]State Key Laboratory of Modern Optical Instrumentation, College of Optical Science and Engineering, Zhejiang University, Hangzhou 310027, China

[d]Theoretical Quantum Physics Laboratory, RIKEN Cluster for Pioneering Research; RIKEN Center for Quantum Computing (RQC), Wako-shi, Saitama 351-0198, Japan; and Department of Physics, University of Michigan, Ann Arbor, Michigan 48109-1040, USA

‡ These authors contributed equally.

* To whom correspondence should be addressed.

E-mail: dgp@scut.edu.cn (G.P. Dong); yangzm@scut.edu.cn (Z.M. Yang)

Supporting Information

S1. Decorated honeycomb-lattice model

We numerically study the topological properties of a finite decorated honeycomb lattice. The lattice consists of 55 sites with alternating hopping strengths t_1 and t_2, as shown in **Figure S1**a. In the tight-binding model, the Hamiltonian of the decorated honeycomb lattice is written as

$$H = \begin{pmatrix} m_A & t_1 & 0 & 0 & 0 & 0 & \cdots \\ t_1 & m_C & t_2 & 0 & 0 & 0 & \cdots \\ 0 & t_2 & m_B & t_2 & t_2 & 0 & \cdots \\ 0 & 0 & t_2 & m_C & 0 & t_1 & \cdots \\ 0 & 0 & t_2 & 0 & m_C & 0 & \cdots \\ 0 & 0 & 0 & t_1 & 0 & m_A & \cdots \\ \vdots & \vdots & \vdots & \vdots & \vdots & \vdots & \ddots \end{pmatrix}, \quad (1)$$

where m_A and m_B denote the masses of the two nonequivalent sites of the honeycomb lattice, m_C denotes the mass of the extra sites inserted from the breathing kagome lattice (see **Figure S1**a). Here we choose $m_A{=}m_B{=}m_C$. In **Figure S1**b, we plot the eigenspectra as a function of t_2/t_1. For $0{<}t_2/t_1{<}1$, there are in-gap corner and edge states, indicating topologically nontrivial phases. While, for $t_2/t_1{>}1$, the in-gap corner and edge states disappear, indicating topologically trivial phases.

S2. Photonic decorated honeycomb lattice

We produced decorated honeycomb lattices using optical waveguide arrays. In the waveguide system, the coupling coefficients c_1 and c_2 can be regarded as the hopping strengths t_1 and t_2, in analogy with electronic systems. These coefficients depend on the separation of two nearest-neighbor waveguides and the excitation wavelength, which can be estimated by $L_c = \pi/2c$. The coupling length L_c denotes the

distance required for the guided modes, in two coupled waveguides, to achieve maximum power conversion. For our configurations, the coupling lengths are L_c = 0.59 cm for d_1 = 12 μm, and L_c = 4.40 cm for d_2 = 12 μm, under the excitation wavelength of 532 nm. Then, the corresponding coupling coefficients are c_1 = 2.66 cm^{-1}, and c_2 = 0.36 cm^{-1}, respectively.

Next, we discuss the topological property of the photonic decorated honeycomb lattice. Electronic higher-order topological systems are characterized by a filling anomaly. For the photonic systems, we can also calculate the filling anomaly and analogous boson charges[1]. The calculation of the analogous boson charges in our photonic lattice follows the following procedure: (1) calculate the local density of states (LDOS) based on the simulated mode distributions of each photonic eigenstate. This LDOS is related to the propagation constant β, which corresponds to the energy in the electronic system; (2) integrate the LDOS to obtain the spectral charge at each unit cell; and (3) the spectral charge distribution is then calculated by summing the entire bulk band.

The calculated results are shown in **Figure1**c of the main text, a fractional corner anomaly $Q = \sigma_{corner} - (\sigma_{edge1} + \sigma_{edge2}) \bmod 1 \approx 1/3$ can be obtained, which indicates the unambiguous identification of higher-order topology.

S3. Slit beam shaping

In our experiments, optical waveguide arrays were fabricated by a femtosecond (fs) laser with a repetition rate of 1 kHz. The power of the pulsed laser is crucial to write high-quality waveguides. When the power is high, it is easy to cause glass damage after laser beam focusing. Moreover, high-power lasers can cause waveguides with a narrow elliptic cross section. This is because the waveguides are

created by transverse writing (the glass sample is translated perpendicularly to the laser beam), and a laser beam with a high peak power can cause the light intensity along the axial direction to be several times stronger than that along the transverse direction when focused into the glass substrate.

To fabricate high-quality waveguides, we use the slit beam-shaping method. The setup of the laser writing is shown in **Figure S2**a. The fs laser beam is focused into a fused quartz glass by a 20× microscope objective with a numerical aperture (NA) of 0.45. An adjustable slit, oriented parallel to the laser's writing direction, is inserted in front of the objective. According to the theory for controlling the laser focal profile[2], the width of the slit is set to 500 μm, in order to shape the fs laser beam. Then we can achieve approximately circular cross-section waveguides, as shown in **Figures S2**b and **S2**c. The waveguide is characterized by a small refractive index difference, 3.3×10^{-4}, between the waveguide and glass matrix, supporting a single-mode guide over the entire visible wavelength range. While the waveguide is fabricated without using a slit, the cross section becomes elliptic, as shown in **Figures S2**d and **S2**e. Note that the waveguide in **Figure S2**d is written using a 10× objective lens, in order to avoid damaging the waveguide.

S4. Bulk and defect states in the Photonic decorated honeycomb lattice

In the main text, we present the corner and edge excitations for different configurations, and the corresponding numerical simulations are shown in **Figure S3**. In addition, we further show the bulk modes in both topological nontrivial and trivial regimes. As shown in **Figure S4**, the bulk II modes, in-between the first and second band gaps, are distributed more extensively than the bulk I modes below the first band gap or above the second band gaps. The experiment results are shown in

Figure S5, consistent with the simulations.

Next, we proceed to explore the effects of defects in the bulk. We designed different bulk vacancies in our system. **Figure S6**a shows the sample of the decorated honeycomb lattice in the presence of two bulk vacancies induced by removing two sites, which are located in the original kagome lattice (type-i defect). By exciting the waveguide closest to the bulk vacancies, we have observed well-localized states at the output facet, as shown in **Figure S6**b. Akin to the corner states in the pristine structure, these modes exist in the bulk gap (see **Figures S7**a,b), because those two vacancies can be regarded as the corner of the triangular sample. **Figure S6**c shows the bulk vacancies introduced by removing one waveguide in the original kagome lattice (type-ii defect) or the original honeycomb lattice (type-iii defect). The type-ii defect introduces the same termination as the edge in the pristine structure, thus supporting a localized state in the triplet (see **Figure S6**d and **Figures S7**c,d). In contrast, when exciting the waveguide nearby the type-iii defect, we observed light diffraction into the bulk (**Figure S6**e).

S5. Effect of defects on edge states

To observe the diffraction behaviors of the edge states in the presence of defects, we fabricated a 10 cm sample with a missing waveguide on the bottom edge, as shown in **Figure S10**a. The excitation diffracts to the next waveguides with triplets, after starting from the excitation site (see **Figure S10**b). This indicates that the excitation can circumvent the defect that does not destroy the “triplets” on the edge. The measured result is consistent with the simulation in **Figure S10**d. Due to the limited waveguide length in our experiment, we also perform numerical simulations for longer propagation distances (see **Figures S10**c-f). As the waveguide length

increases, the edge state can pass through the defect, and eventually distributes over the entire edge at z=70 cm. The animation of the dynamic evolution process is given in Supplementary Video 1.

Furthermore, we produced additional two-site defects by removing the waveguides at different positions, as shown in **Figure S11**. These defects destroy the triplets at the edge. The simulated dynamical evolutions of light in waveguide arrays show that the edge diffractions are blocked by the defects, and can only transport along the direction without defects. The animations of the dynamic evolution process are given in Supplementary Videos 2 and 3. Note that the directional diffraction behaviors of edge states in this system should be distinguished from chiral propagation.

S6. Robustness of the corner states

To study the robustness of the higher-order corner states, we study different types of disorder, which either preserve or break the C_3 and chiral symmetries.

For the C_3-preserving case, the disorder is applied to the coupling coefficients c_2 with the modified coupling $c'_2=c_2+\alpha$, as shown in **Figure S12**a. Here, $\alpha \in [-W/2, W/2]$ is a uniformly distributed coupling term. **Figure S12**b shows eigenspectra as a function of the disorder strength δ. Here, the standard deviation $\sigma=W/\sqrt{12}$ of uniformly distributed random numbers is used to evaluate the disorder strength δ: $\delta=\sigma/C$, with $C=(c_1+c_2)/2$. The energies of the corner states are insensitive to the C_3-preserving disorder for a finite-disorder strength. In contrast, when the disorder is stochastically applied both to the coupling coefficients c_1 and c_2 with the modified values $c'_{1,2}=c_{1,2}+\alpha_i$, with $i \in [1, 5]$ (see **Figure S12**a), C_3 symmetry is broken and the energies of the corner states are strongly influenced, as shown in

Figure S12c. In this case, the corner states are coupled to the bulk modes.

Furthermore, the robustness of the corner states can be quantified by calculating the averaged mean squared difference between the energy of the disordered system and the one without disorder. The localization of the corner modes can be characterized by the inverse participation ratio[3] (IPR), which is defined as

$$\mathrm{IPR} = \frac{\sum_{i=1}^{N} |\psi_{i,\beta_{\mathrm{corner}}}|^4}{\left(\sum_{i=1}^{N} |\psi_{i,\beta_{\mathrm{corner}}}|^2\right)^2} \tag{2}$$

where $\psi_{i,\beta_{\mathrm{corner}}}$ denotes the normalized wave function amplitude of corner states at the site i. Here, the IPR is averaged over all eigenstates of the corner states. Our results are presented in **Figure 4** in the main text, which show that the corner states in the photonic square-root HOTI are protected by the C_3 symmetry.

In addition to the C_3 symmetry, the Hamiltonian on a decorated honeycomb lattice also preserves chiral symmetry, i.e., H satisfies $\gamma H \gamma^{-1} = -H$, where

$$\gamma = \begin{pmatrix} 1 & 0 & 0 & 0 & 0 \\ 0 & 1 & 0 & 0 & 0 \\ 0 & 0 & -1 & 0 & 0 \\ 0 & 0 & 0 & -1 & 0 \\ 0 & 0 & 0 & 0 & -1 \end{pmatrix}. \tag{3}$$

We now consider the chiral-breaking disorder schemes applied to the next-nearest-neighbor coupling (**Figure S13**a) or on-site potentials (**Figure S13**d). For both cases, the C_3 symmetry is preserved. We present the eigenspectra (**Figure S13**b,e) and the energy fluctuations (**Figure S13**c,f) of the corner states as a function of the disorder strength. The results indicate that the corner states are robust against chiral-breaking disorder that preserves the C_3 symmetry.

S7. Nonlinear properties of the square-root higher-order topological insulator

To understand the nonlinear properties of our photonic square-root HOTI, we

have simulated light dynamics under both linear and nonlinear excitations, as shown in **Figure S14**. For the linear excitation, the localized corner states are clearly observed only in the topologically nontrivial regime. When nonlinear interactions are introduced, corner-excitation modes tend to be localized both in the homogenous and topologically trivial regimes. And well-localized corner solitons are formed in the strong nonlinear regime[4]. Surprisingly, weak nonlinearity leads to a small coupling of the original corner modes to bulk states in the topologically nontrivial regime. Increasing the nonlinearity induces a tight localization in the corner sites. These results in square-root HOTIs are similar to the nonlinear properties in conventional HOTIs[5,6].

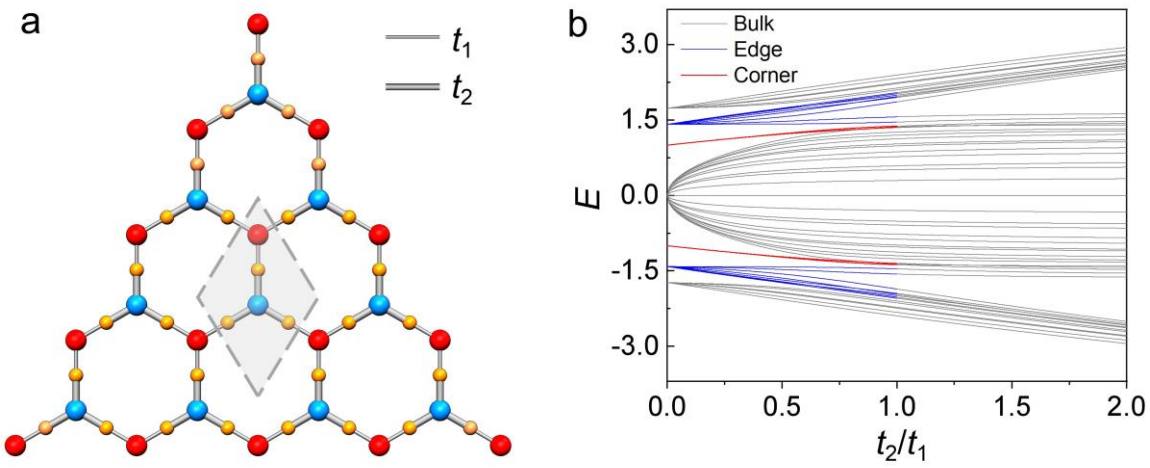

Figure S1. Lattice and band structures of the square-root higher-order topological insulators studied here. (a) Schematic of the decorated honeycomb lattice. The dashed gray rhombus denotes the unit cell, which consists of two nonequivalent sites (red and blue solid balls) contributed from the honeycomb-lattice, and three extra-inserted sites (orange solid balls) from the breathing kagome lattice. The hopping strengths are denoted by t_1 and t_2. (b) Eigenenergy E versus t_2/t_1. The gray, blue, and red curves denote the bulk, edge, and corner states, respectively.

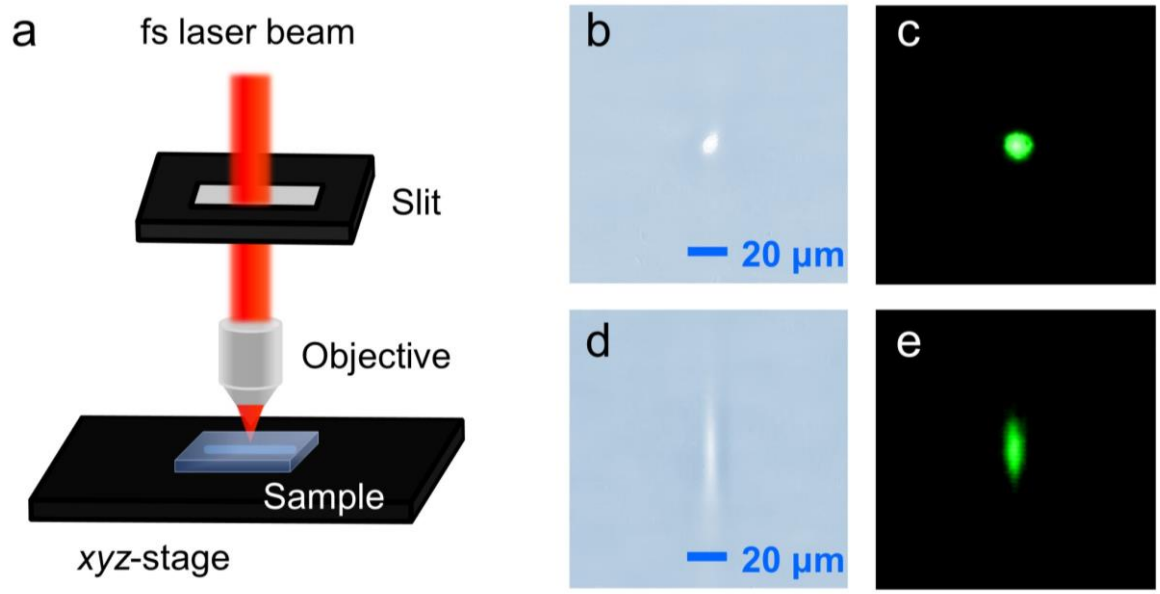

Figure S2. Slit beam shaping. (a) Schematic of the experimental setup for fabricating waveguides with approximate circular cross-section using the slit-beam-shaping method. (b) White-light transillumination image of waveguides fabricated in the fused quartz glass with 20×(NA 0.45) objective lens and slit width of 500 μm. (c) Near-field intensity distribution of the guided mode in (b) excited by light with a wavelength of 532 nm. (d) White-light transillumination image of waveguides fabricated in the fused quartz glass with 10×(NA 0.3) objective lens but without the slit beam shaping. (e) Near-field intensity distribution of the guided mode in c excited by light with a wavelength of 532 nm. The image in (b) and (d) is on a 1:1 scale with the experimental images in (c) and (e), respectively.

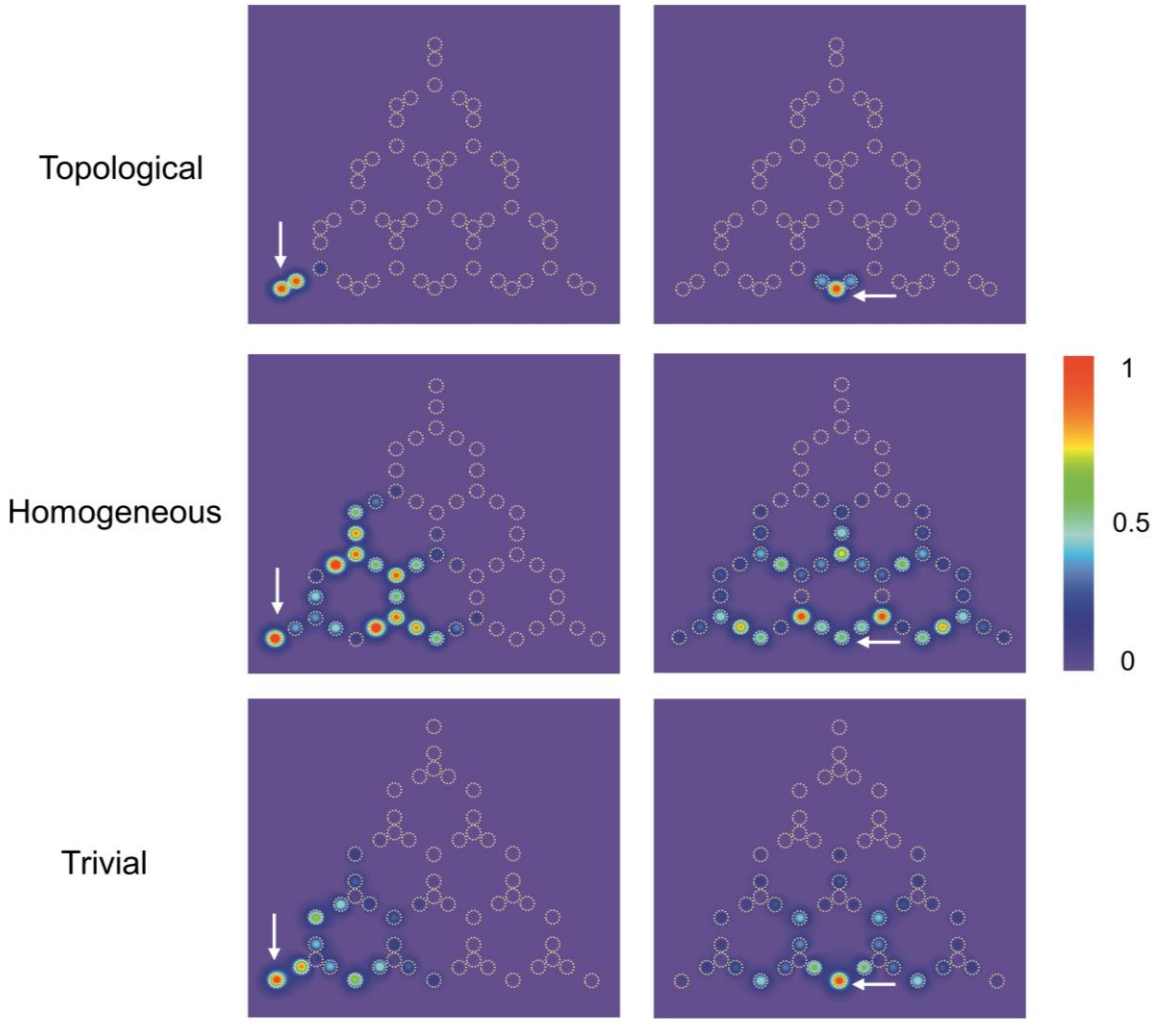

Figure S3. Simulated intensity distributions of the decorated honeycomb lattices in the topologically nontrivial, homogeneous, and topologically trivial regimes, subject to corner/edge excitations.

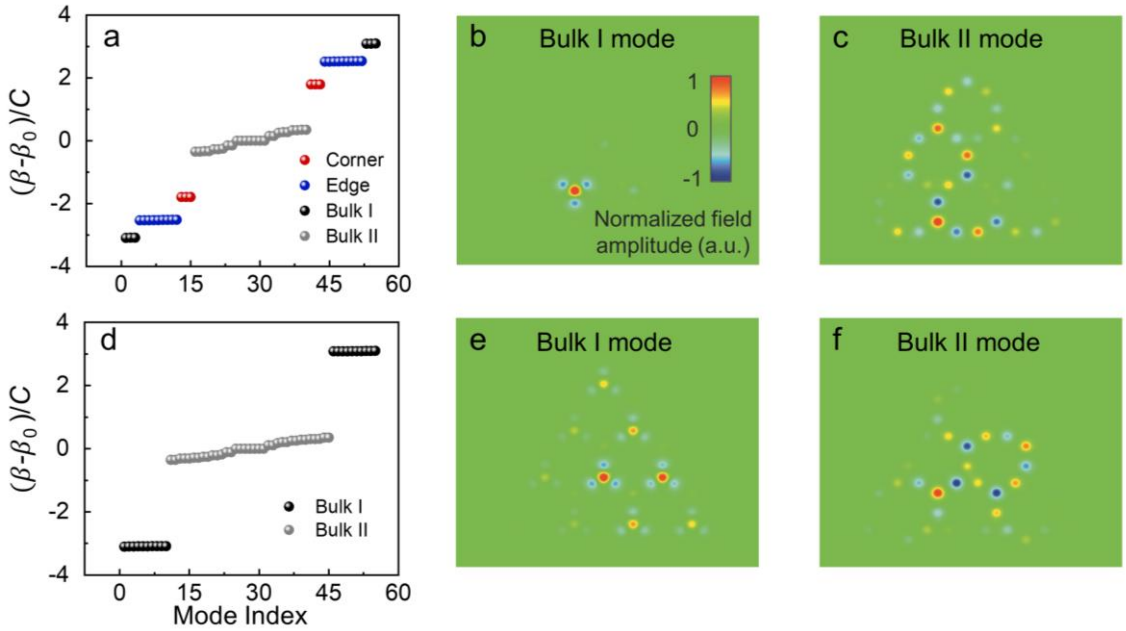

Figure S4. Calculated eigenspectra of the finite waveguide arrays. Two typical bulk mode distributions (labelled as bulk I and II) (a-c) in the topologically nontrivial regime, and (d-f) in the topologically trivial regime.

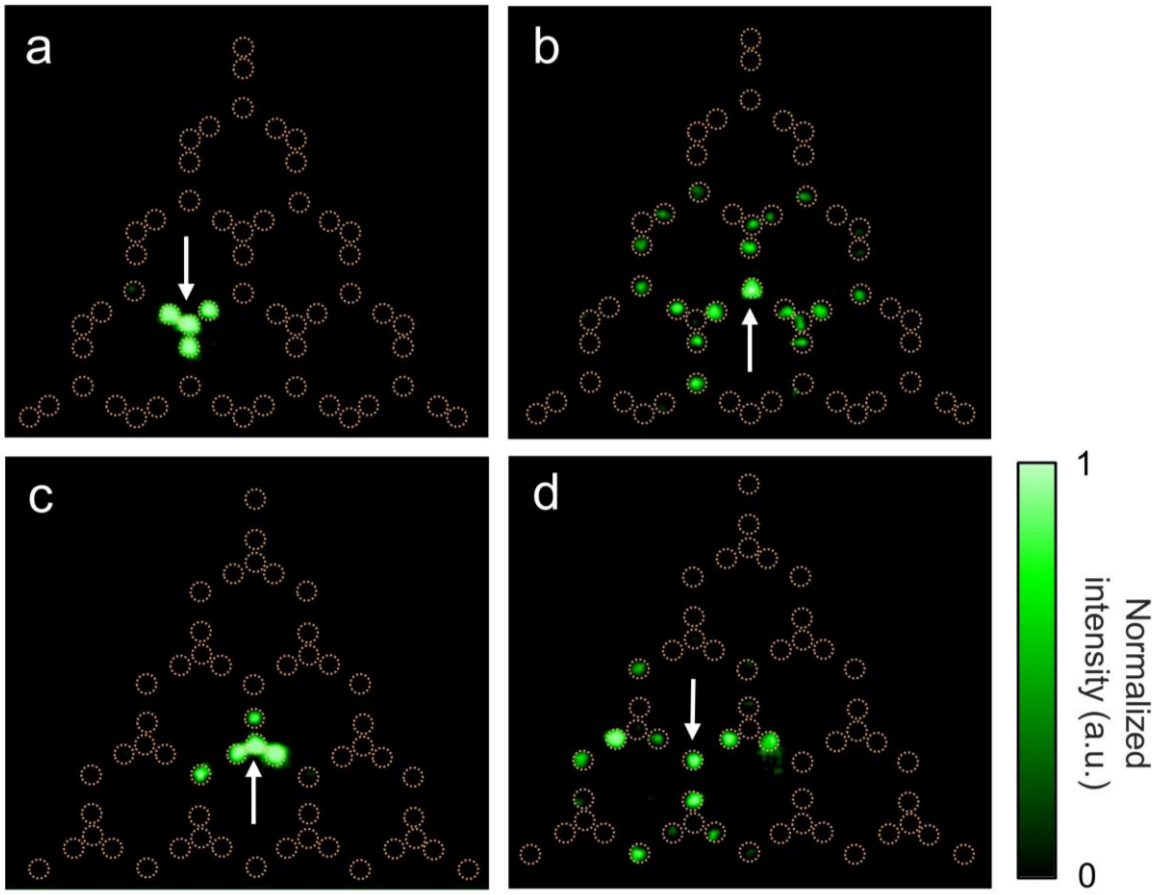

Figure S5. Experimental images of light emerging at the output facet of the waveguide array with length z = 49 mm in (a, b) topologically nontrivial and (c, d) trivial regimes, corresponding to the simulated bulk mode distributions. Light of wavelength 532 nm is injected into the bulk waveguide (indicated by a white arrow).

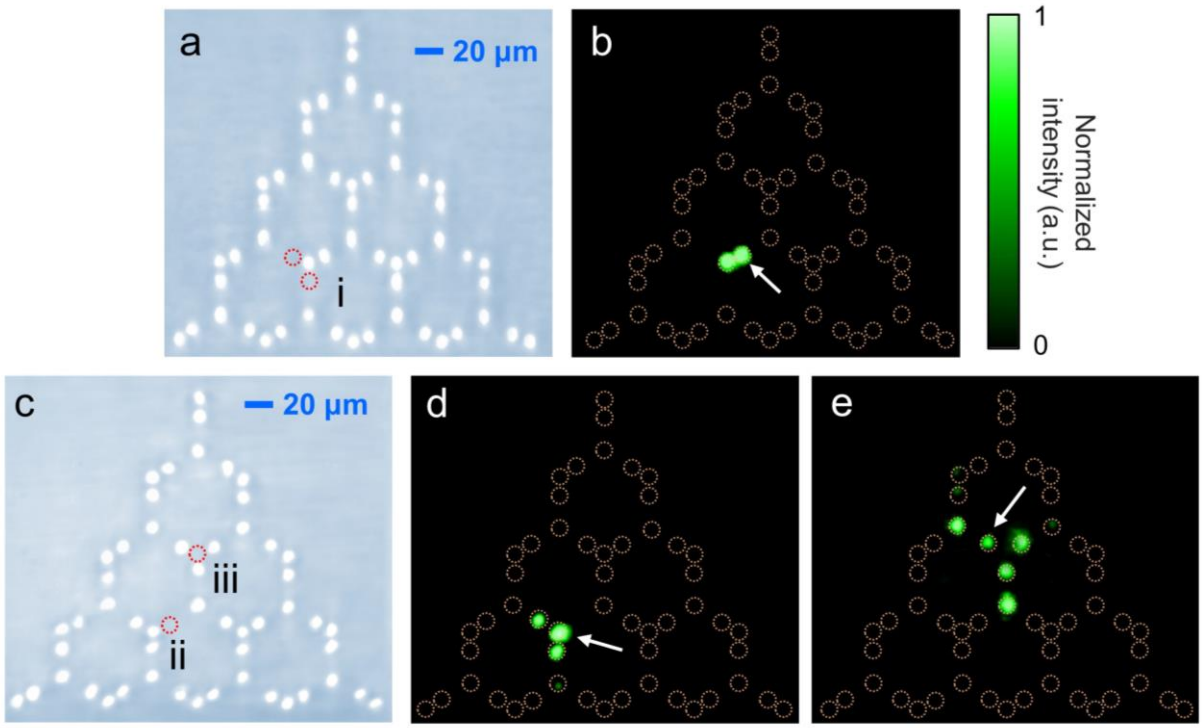

Figure S6. Measured results of bulk-defect modes. (a, c) Microscope images of the waveguide arrays with different types of bulk vacancies marked by red dotted circles. (b, d) and e show experimental images of light emerging at the output facet of the waveguide array corresponding to the type-i, ii, and iii defects, respectively.

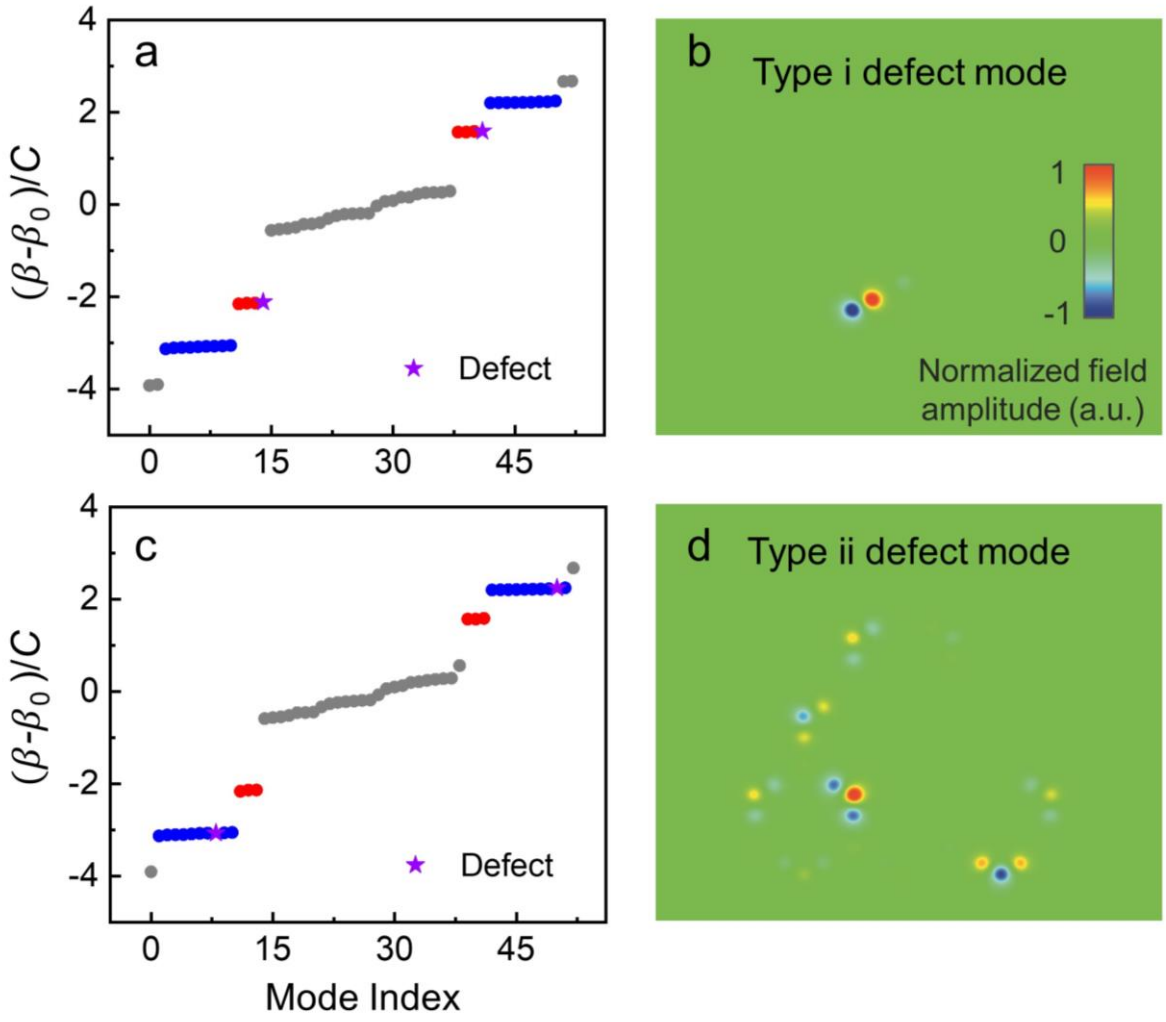

Figure S7. Calculated eigenspectra and defect mode distributions (a, b) for type-i bulk vacancies and (c, d) for the type-ii defect.

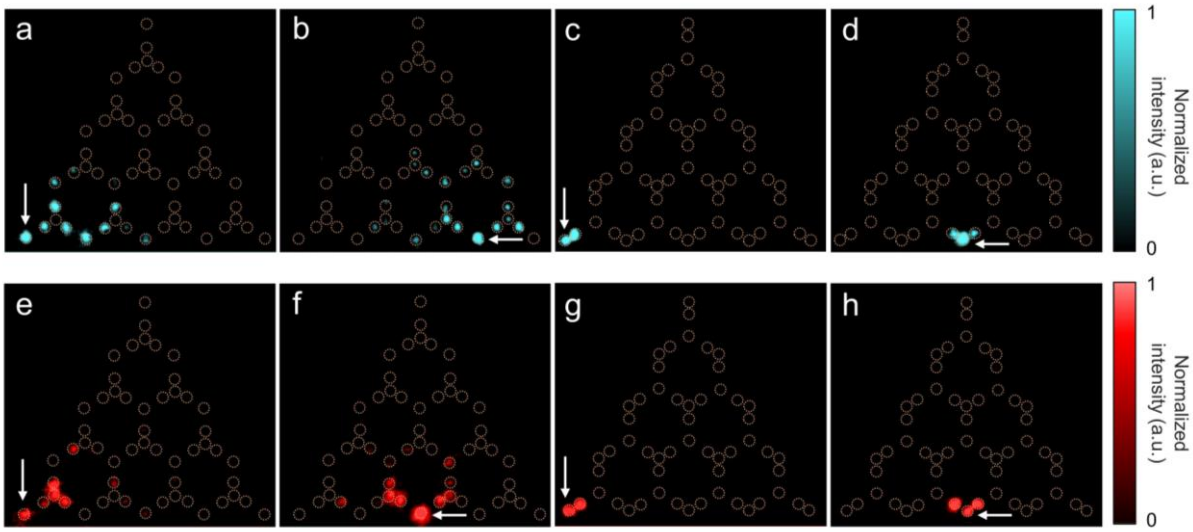

Figure S8. Square-root higher-order topological insulator with different coupling distances. (a-d) Experimental images of light emerging at the output facet of the waveguide array for $d_{1/2}$=18 μm and $d_{2/1}$=11 μm ($c_{1/2}$=0.35 cm^{-1} and $c_{2/1}$=2.76 cm^{-1}). Light at wavelength 447 nm is injected into the waveguide at the corner (a, c) and edge (b, d) Also, the panels (e-h) show the experimental images of light emerging at the output facet of the waveguide array for $d_{1/2}$=25 μm and $d_{2/1}$=13 μm ($c_{1/2}$=0.41 cm^{-1} and $c_{2/1}$=2.71 cm^{-1}). Light at wavelength 633 nm is injected into the waveguide. The light diffracts into the bulk for the topologically trivial phases, but are confined at the corner or edge for the topologically nontrivial phases.

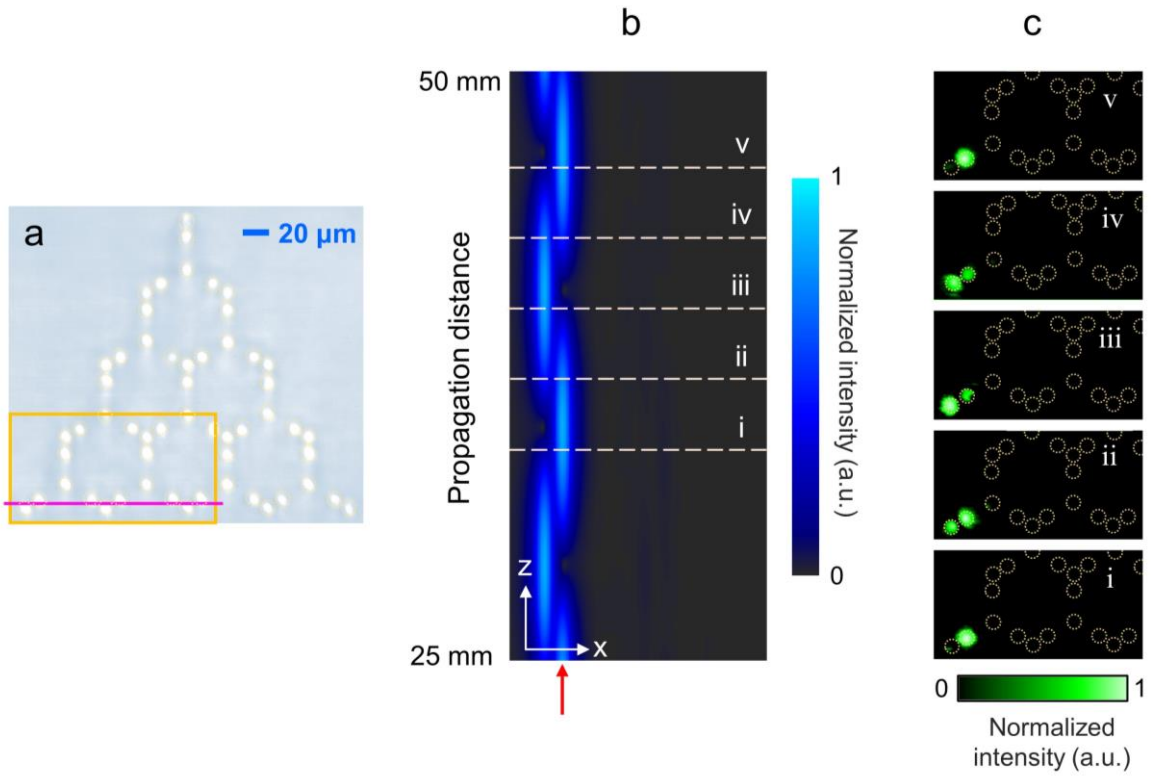

Figure S9. Dynamical evolution of the corner modes by exciting the second waveguide at the bottom left corner. (a) Microscope image of the decorated honeycomb lattice. White-light transillumination image captured from the output end facet (*xy* plane) of the waveguide array. The two characteristic distances between nearest-neighbor waveguides are d_1=12 μm and d_2=21 μm. (b) Numerical simulation of the light propagation when exciting the second waveguide (see Figure S10a) at the bottom left corner. The red arrow at the bottom indicates the position of the light injection. The *y*-section is located between the first and second rows of the waveguide array (marked by the violet line in (a)). The panels i-v correspond to waveguides with lengths of z = 34, 37, 40, 43, 46 mm. (c) Measured light distributions (orange rectangles in (a)) at the output facet from i to v.

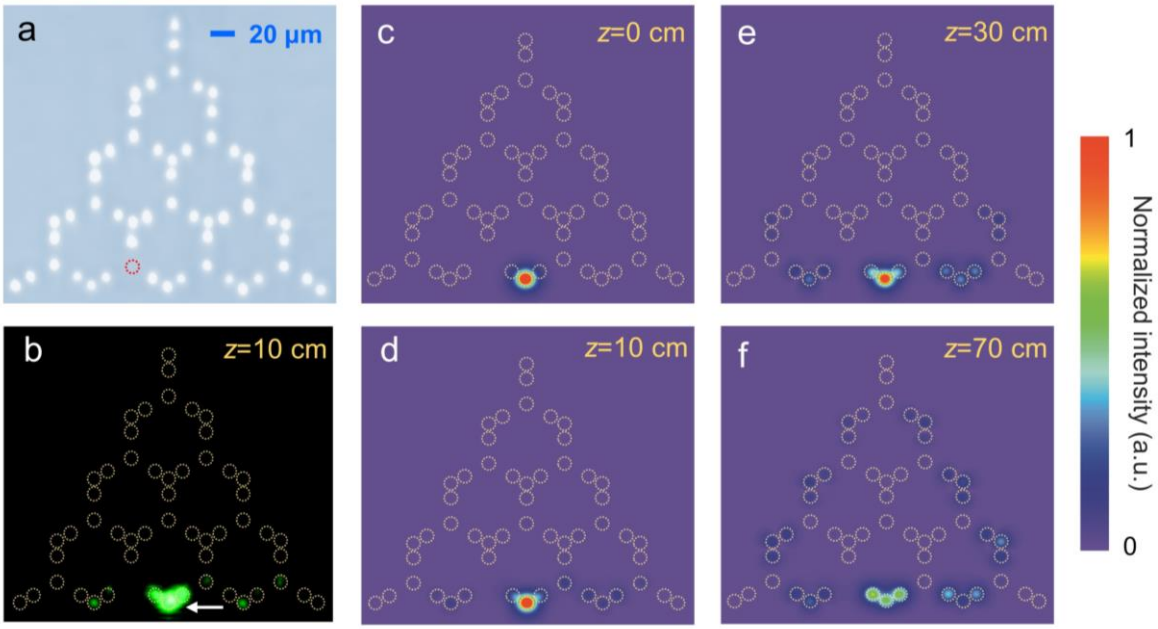

Figure S10. Effect of defects on edge states. (a) Microscope image of the waveguide array with a missing waveguide (marked by a red dotted circle in panel (a)) on the edge. (b) Experimental image of light emerging at the output facet of the waveguide array with the defect (z = 10 cm). The light is injected into the waveguide on the bottom edge (indicated by a white arrow). (c, d) Simulations of light diffraction through the waveguide array at various propagation distances with z = 0, 10 cm, 30 cm, and 70 cm, respectively. The experimental result in (b) is consistent with the simulated result in (d).

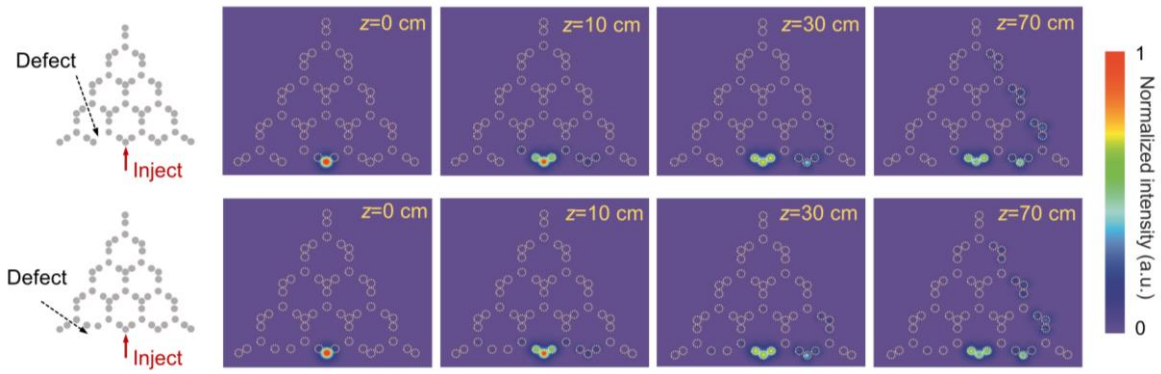

Figure S11. Simulated results of the light diffraction through the waveguide array with two kinds of edge defects (left panel) at various propagation distances z = 0, 10 cm, 30 cm, and 70 cm, respectively. The defects suppress the light on the triplets at the edge; thus, the edge states can only propagate along the direction without defects. The diffraction behaviors of edge states in this system should be distinguished from chiral propagation.

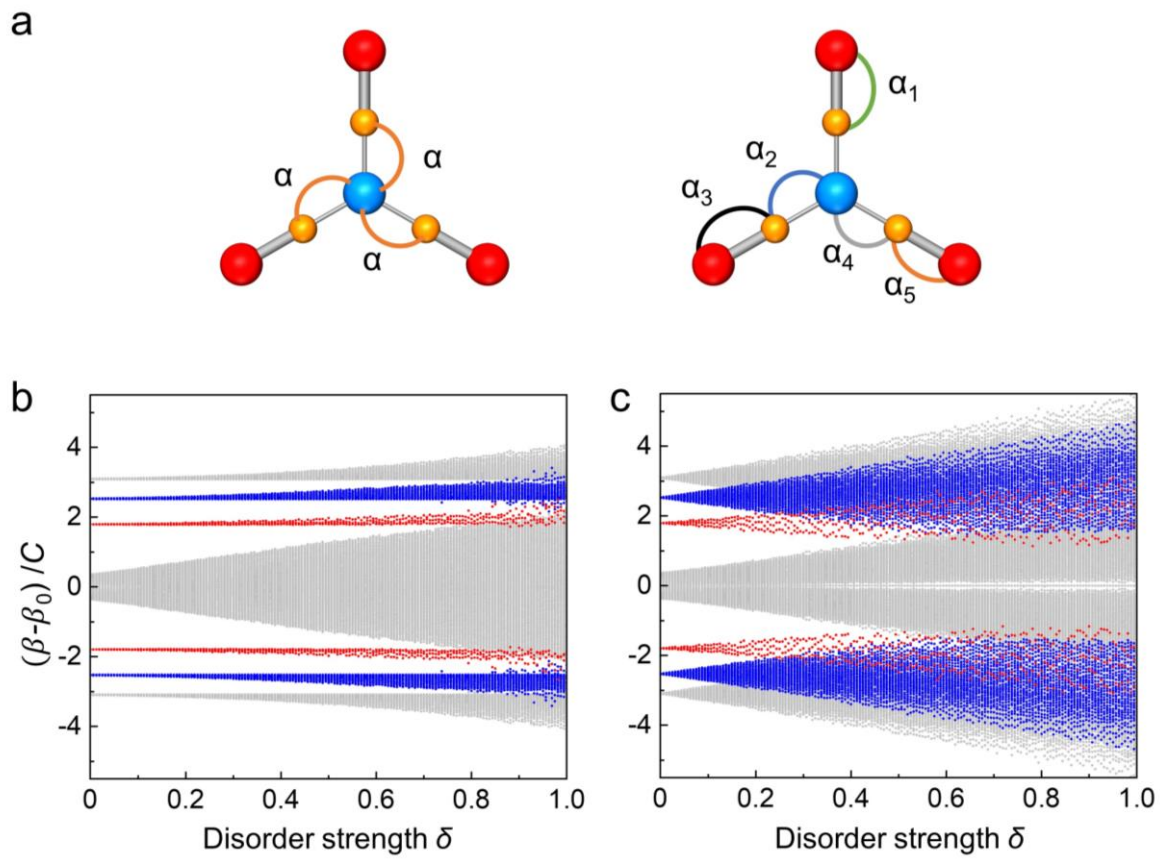

Figure S12. Robustness analysis of corner states against C_3-breaking disorder. (a) Schematic showing the type of disorder that preserves (left panel) and breaks (right panel) C_3 symmetries (marked by the colored arcs). (b, c) Eigenspectra of the corner (red dots), edge (blue dots) and bulk (black bots) states as a function of the disorder strength δ for the (b) C_3-preserving and (c) C_3-breaking disorder scheme.

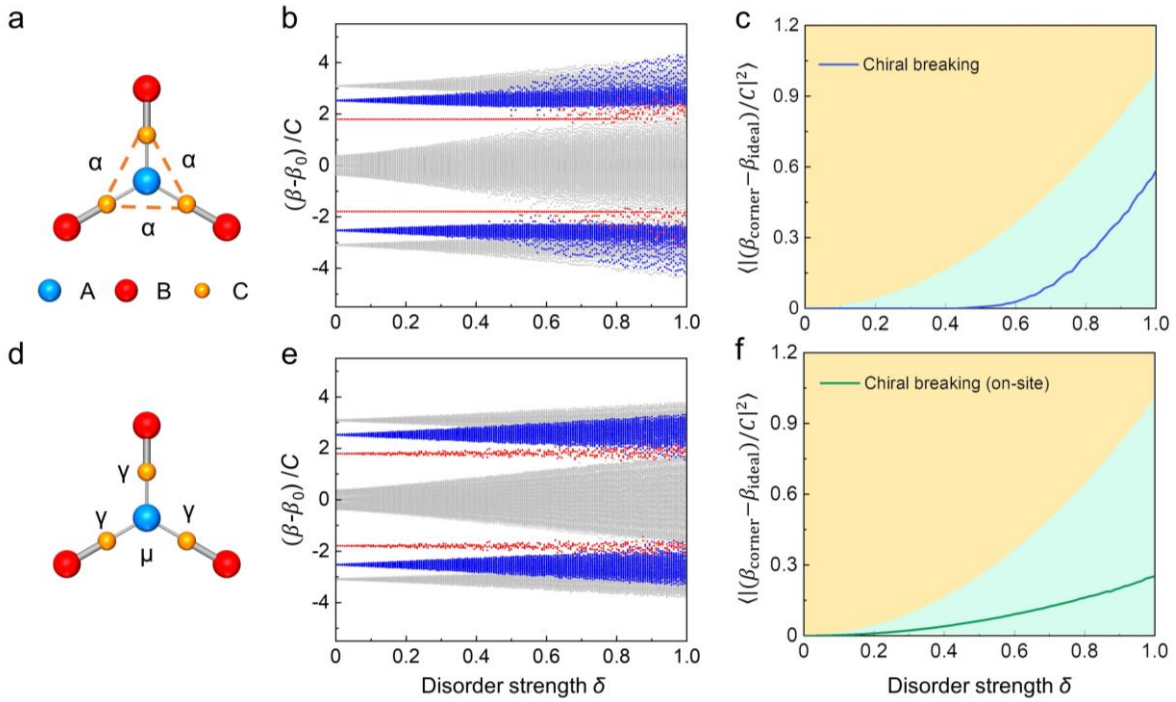

Figure S13. Robustness analysis of corner states against chiral-breaking disorder. (a) Schematic showing the disorder applied to the next-nearest-neighbor coupling (marked by the dotted orange line). (b) Eigenspectra as a function of δ for the disorder in (a). (c) Energy fluctuation of the corner states as a function of δ for the disorder in (a). The vertical axis denotes the averaged mean squared difference between the energy β_{corner} of the corner state in the disordered system and the corner-state energy β_{ideal} in the ideal or clean system. (d) Schematic showing the disorder applied to the on-site potentials with μ and γ added on the sites A (blue pellets) and C (orange pellets), respectively. (e, f) same as (b, c) but for the disorder in (d).

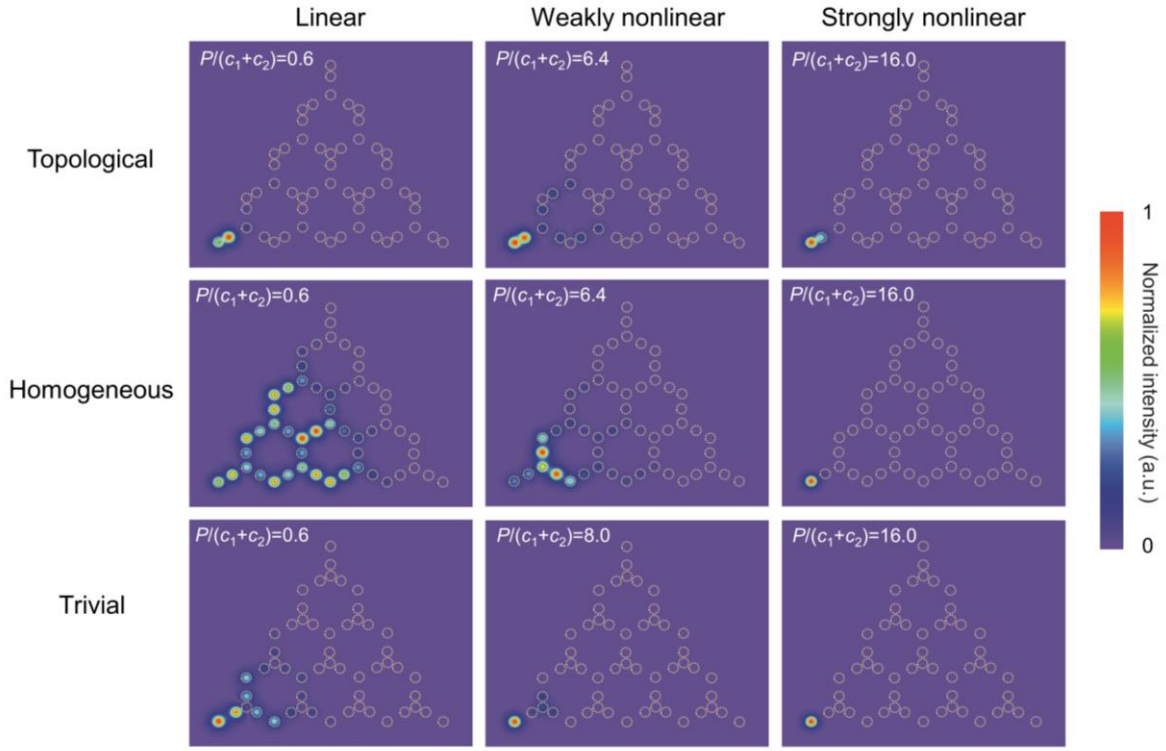

Figure S14. Simulated light dynamics of decorated honeycomb lattices in linear and nonlinear regimes under corner excitations. Upper, middle and bottom rows show the light output patterns for different input powers in the topologically nontrivial, homogeneous, and topologically trivial regimes, respectively. Here, $P/(c_1+c_2)$ represents the normalized power.

References

[1] S. Wu, B. Jiang, Y. Liu, and J. Jiang, All-dielectric photonic crystal with unconventional higher-order topology, *Phys. Rev. Research* **9**, 668-677 (2021).

[2] Z. Zeng, N. Ling, and W. Jiang, The investigation of controlling laser focal profile by deformable mirror and wave-front sensor, *J. Mod. Opt.* **46,** 341-348 (1999).

[3] B. Kramer and A. Mackinnon, Localization: theory and experiment. *Rep. Prog. Phys*. **56**, 1469-1564 (1993).

[4] A. Szameit, Y. V. Kartashov, F. Dreisow, T. Pertsch, S. Nolte, A. Tunnermann, and L. Torner, Observation of two-dimensional surface solitons in asymmetric waveguide arrays, *Phys. Rev. Lett.* **98**, 173903 (2007).

[5] D. Smirnova, D. Leykam, Y. Chong, and Y. Kivshar, Nonlinear topological photonics, *Appl. Phys. Rev.* **7**, 021306 (2020).

[6] M. S. Kirsch, Y. Zhang, M. Kremer, L. J. Maczewsky, S. K. Ivanov, Y. V. Kartashov, L. Torner, D. Bauer, A. Szameit, and M. Heinrich, Nonlinear second-order photonic topological insulators, Nat. Phys. **17**, 995 (2021).